Characterization of a Low-Cost, Monolithically Integrated, Tunable 10G Transmitter for Wavelength Agile PONs

Daniel Carey , *Student Member, IEEE,* Prasanna Ramaswamy, *Student Member, IEEE,*
Giuseppe Talli , *Member, IEEE,* Cleitus Antony , *Member, IEEE,*
Brendan Roycroft, Brian Corbett, and Paul D. Townsend, *Member, IEEE*

***Abstract*— Dynamically reconfigurable passive optical networks (PONs) using time-division multiplexing and dense wavelength division multiplexing will require low-cost, high-performance customer premises equipment to be economically viable. In particular, substantial cost savings can be achieved through the use of efficient re-growth free, foundry-compatible fabrication techniques. Using this strategy, this paper presents the first detailed characterization of a monolithically integrated transmitter comprised of a discretely tunable slotted Fabry–Pérot ridge waveguide laser, an absorptive modulator and a semiconductor optical amplifier (SOA) produced using a standard off-the-shelf AlInGaAs/InP multiple quantum well epitaxial structure. This first generation device demonstrates a discrete single-mode tuning range of approximately 12 nm between 1551nm and 1563 nm with a side-mode suppression ratio ≥ 30 dB. Moreover, the integrated modulator section is shown to support transmission at 10 Gb/s using non-return to zero on-off keying with an extinction ratio in excess of 8 dB. Furthermore, using a time-resolved chirp measurement technique to examine dynamic deviations in the set carrier frequency, the modulator section exhibits a chirp contribution of < 6 GHz using test patterns with high and low frequency content. In addition, the generation of optical bursts through the application of a gating function to the SOA section was found to shift the unmodulated carrier of a typical lasing mode by ≤ 8 GHz for gating periods comparable with a typical PON burst durations of 125 μs which are faster than the thermal response time of the transmitter material.**

***Index Terms*— Optical communications, dense wavelength division multiplexing, time division multiplexing, passive optical networks, tunable semiconductor lasers, monolithic integration.**

I. Introduction

LOW-COST, widely tunable transmitters with a high-bandwidth capability (≥ 10Gb/s) will be a key requirement for "colorless" optical network units (ONUs) located at the customer's premises within dynamically reconfigurable time-division multiplexed (TDM) and dense wavelength division multiplexed (DWDM) passive optical networks (PONs) [1]. In particular, these transmitters will require a high-level of tuning precision and wavelength stabilization in order to maintain the integrity of the set transmission channel and avoid inter-channel crosstalk. A consequence of the strict tolerance placed on the accuracy and precision of the transmission wavelength coupled with the need for a wide tuning range (>10nm) demands a greater design and fabrication complexity; therefore, cost becomes a critical factor for these components.

In practice, monolithic integration eliminates the challenging design and fabrication processes necessary for hybrid transmitter assemblies by achieving the desired multi-component functionality on a single chip resulting in a reduced form factor, power consumption and cost. Today, monolithically integrated tunable lasers are typically variants of the distributed Bragg reflector (DBR) laser, such as the sampled grating [2], super structure grating [3] and digital supermode DBR lasers [4]. Other types of tunable laser such as the modulated grating Y-branch (MG-Y) laser are based on interferometric principles using Y-couplers [5]. Alternatively, various types of tunable external cavity lasers (ECLs) have been designed [6], while a promising device based on a vertical-cavity surface emitting laser (VCSEL) using a surface micro-machined, electro-thermally actuated upper mirror has been shown to achieve a continuous single-mode tuning range of 102 nm [7]. The main disadvantage of these devices is their complex fabrication process which includes multiple epitaxial growths requiring high tolerance steps for creating the grating structures which can lead to high production costs. However, by taking inspiration from the cleaved coupled-cavity (C3) lasers demonstrated in [8] and the Y-laser presented in [9], designs for potentially low-cost discretely tunable lasers have been developed over the course of last decade by etching slots into Fabry-Pérot (FP) ridge waveguide lasers [10]. Notably, within these devices, the slots are only etched through the upper waveguide and not through the active quantum well region. Moreover, as the slots are etched in the same step as the waveguide there is no additional fabrication complex- ity required to facilitate partial electrical isolation between

This work was supported in part by the Science Foundation Ireland under Grant 12/IA/1270 and Grant 12/RC/2276 and in part by the EU FP7 Integrated Project DISCUS under Grant CNECT-ICT-318137. *(Corresponding author: Daniel Carey.)*

The authors are with the Tyndall National Institute, University College Cork, Lee Maltings, Cork, T12R5CP Ireland (e-mail: daniel.carey@tyndall.ie).

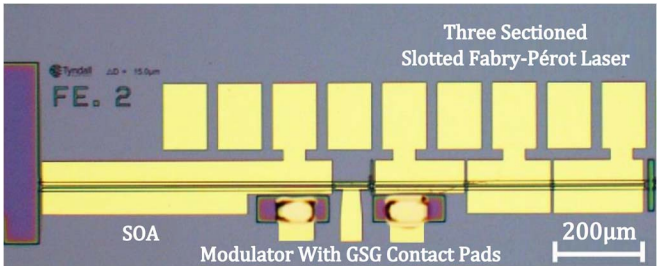

Fig. 1. Optical microscope image of the monolithically integrated transmitter with a total length of approximately 1.4mm incorporating a three-sectioned discretely tunable slotted Fabry-Pérot ridge waveguide laser (616 μm), modulator (80μm) and an SOA (675μm).

sections. The slots serve to introduce reflections within the laser cavity which perturb the primary longitudinal mode; this results in mutually coupled FP cavities. By injecting currents into each section the local gain and refractive index can be altered to control the overall gain and phase resonances thereby achieving tunability from the device. It is important to note that these slotted Fabry-Pérot (SFP) lasers require only a single epitaxial growth process and standard lithography techniques which offer major advantages by greatly reducing the fabrication complexity while also increasing the potential yield. Furthermore, as these lasers do not explicitly need cleaved facets to form the laser cavity they can be employed to integrate monolithically with other optical devices such as absorptive modulators or semiconductor optical amplifiers (SOAs) through the implementation of deeply etched facets.

In this work, we present the first iteration of a 10G-capable optical transmitter consisting of a discretely tunable three-sectioned (3s) SFP laser that has been mono- lithically integrated with an absorptive modulator and an SOA using foundry-compatible fabrication methods that offer the potential for low-cost mass production. The following section briefly outlines the transmitter design and fabrication process, while section III presents the primary characterization results alongside the impact of inter-section crosstalk and the continuous-mode (CM) transmission performance at 10Gb/s using non-return-to-zero on-off keying (NRZ-OOK). Finally, in section IV, a time-resolved chirp measurement technique is used to determine the wavelength stability of the transmitter under modulation as well as various SOA gating conditions in order to examine the implications for the set carrier frequency during the generation of optical bursts.

II. Device Design and Fabrication

The integrated transmitter chip was fabricated using a single epitaxial growth process and standard lithography techniques with a standard off-the-shelf AlInGaAs/InP structure comprised of multiple quantum wells on an n-doped substrate.

As shown in Fig. 1, the length of the laser was defined using deeply (5μm) etched facets. The light produced by the laser is guided using a surface ridge with three separately contacted sections of slightly different lengths, 210μm, 192μm and 212μm, each divided by a shallow etched slot as shown in Fig. 2 (c) and (d). These partially reflective 1μm-wide slots with a depth of 1.85μm are defined in the same step as the

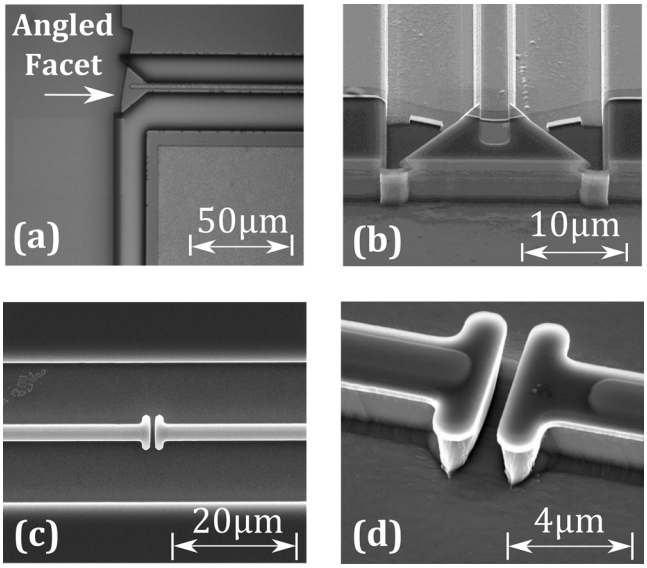

Fig. 2. a) Scanning Electron Microscope (SEM) image of a deeply etched facet which is angled with respect to the ridge for reduced optical feedback in the SOA section b) Facet view of the ridge, c) a shallow slot etched into the ridge waveguide of the integrated laser (d) tilted view of an etched slot.

ridge waveguide. Therefore, they present no additional complexity in the fabrication process. During operation, reflections from these slots cause interference and by varying the drive current to each section, the gain and index of each section of the laser can be controlled such that single-mode lasing is achieved.

The integrated modulator is an in-line absorbing section with a length of 80μm that is accessed through a ground-signal-ground (GSG) contact pad for which no effort was made to reduce the pad capacitance in this initial implementation. The input facet of the modulator section was separated from the laser output by 15μm using a deep etch (5μm) with an angle of 7° with respect to the ridge in order to mitigate back reflections while the output facet was separated from the 675μm long SOA section with a shallow, 1μm-wide angled slot. As shown in Fig. 2 (a) and (b), the output facet of the integrated SOA was lithographically etched with an angle of 7° with respect to the ridge to reduce undesirable optical feedback. It is important to note that the use of lithographic etching in the fabrication process eliminates cleave errors and ensures that the dimensions of all the elements on the wafer are well controlled. Since all the integrated components operate at the same bandgap, the fabrication process is completely regrowth-free and foundry-compatible which is expected to greatly reduce the cost of the devices.

III. Transmitter Characterization

As shown in Fig. 3, this first generation monolithically integrated transmitter chip was characterized in an unpackaged state using a probe station which consisted of a temperature controlled sub-mount, a 40GHz GSG RF probe, a multi-contact DC wedge probe and a lensed single-mode fiber (SMF) into which the light was coupled via free-space alignment using an XYZ translational stage.

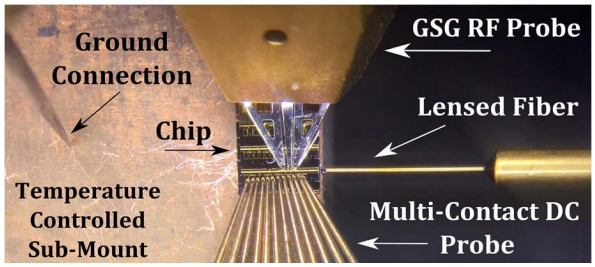

Fig. 3. Microscope view of the probe station setup showing the integrated transmitter chip, RF GSG probe, multi-contact DC probe and lensed fiber.

A. Laser Section

To examine the relation between the tuning currents and the peak transmission wavelength, a coarse calibration of the transmitter was performed by varying the bias currents supplied to each section of the SFP laser in steps of 5mA and examining the resultant spectra using an optical spectrum analyzer (OSA). The results of this calibration, shown in Fig. 4, indicate a discrete tuning range of approximately 12nm between 1551 and 1563nm which has been defined using a side-mode suppression ratio (SMSR) threshold of 30dB as required by the NG-PON2 standard (G.989.2) [11]. Moreover, as outlined in [12], the primary mode spacing within these lasers is determined by the overall length of the laser cavity (~616μm) with every third mode being preferentially selected due to the sectioning of the cavity. This corresponds to a mode spacing of roughly 200GHz; however, a smaller spacing can be achieved by increasing the length of each section and vice versa. Nonetheless, due to the Vernier effect, only a single mode from the sets of cavity modes can be aligned; therefore, any unintended variations in the actual length of the sections will result in a shift in the tuning map with respect to the applied current. It is also important to note that the resonance conditions are dependent on the refractive indices of the individual sections which in turn are temperature dependent, therefore, the achievable modes are not strongly predictable at present. As a result, the information presented in Fig. 4(a) is included purely for indicative purposes. However, for further information on the tuning mechanisms of these lasers the reader is directed to [13]. Additionally, since the applied tuning currents also manipulate the gain within each section of the laser, there will be an appreciable peak-power variation across the tuning range. For instance, in the device reported in this work, the power variation across the specified tuning range was measured to be approximately 7.5dB, hence, it is expected that the integrated SOA could be used to equalize the power between the different selected lasing wavelengths.

Lastly, in order to fill in the spectral gaps evident in Fig. 4(b), fine-tuning can be accomplished by adjusting the granularity of the tuning currents and by varying the chip temperature as demonstrated in [14]. However, it should be noted that this mechanism is limited since a significant variation in the refractive index can alter the resonance conditions causing the present lasing mode to hop to a different mode. Nonetheless, to demonstrate the single-mode operation of the transmitter, the spectral profile of 10 arbitrarily chosen tuning settings are presented in Fig. 4(c), which exhibit a positive

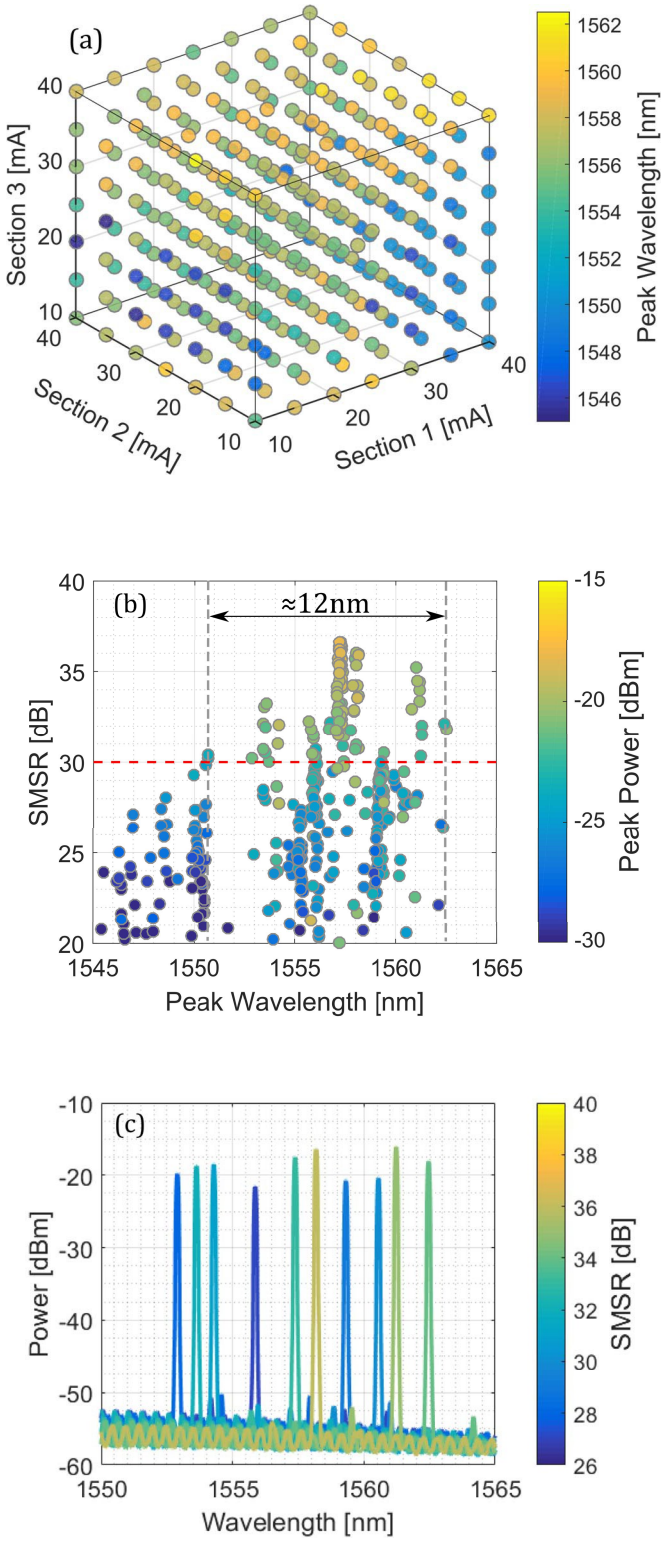

Fig. 4. Coarse calibration: (a) Tuning map recorded using 5mA steps, (b) SMSR of the achieved lasing modes plotted against the peak wavelength, (c) Optical spectra of 10 discrete lasing modes with SMSR > 30dB. [Modulator bias = −1.0V, SOA bias = 30mA and T = 20°C]

detuning from the material gain peak (~1542nm), where the modulator and SOA sections are biased at −1.0V and 30mA respectively while the submount temperature is set at 20°C.

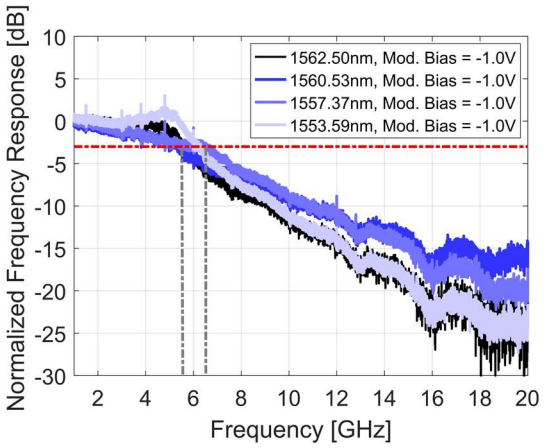

Fig. 5. Normalized small-signal frequency response of the integrated transmitter for four arbitrarily chosen lasing modes [SOA bias = 30mA, T = 20°C].

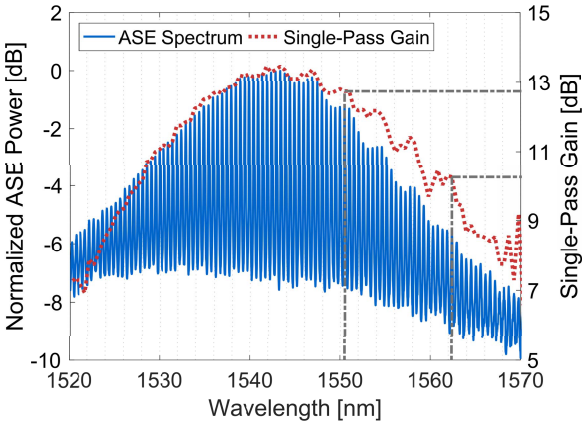

Fig. 6. Normalized ASE spectrum and the corresponding single-pass gain generated by the integrated SOA section for an applied bias current of 30mA and an estimated facet reflectivity ($R_1 \approx R_2$) of 0.02. [OSA resolution = 0.1nm, T = 20°C]

B. Modulator Section

As outlined in section II, the modulator section fabricated within this test device was simply an 80μm-long absorbing section accessible through a GSG contact pad. This approach was taken in order to examine the feasibility of integrating the 3s-SFP laser with other electro-optic components and to investigate the potential high-speed capabilities of the envisaged transmitter. However, in the absence of quantum well intermixing (QWI) [15], the trial modulator structure exhibited an undesirably high level of loss (~20dB), as detailed in Section III-C). Moreover, when this f0eature was combined with the fiber coupling loss, an external optical amplifier was required during the characterization process in order to achieve powers comparable with commercial devices (+5dBm). Nonetheless, to determine the modulation capability of this section, the small-signal frequency response was recorded for various laser tuning settings using a vector network analyzer (VNA) and a calibrated high-speed photo-receiver. The results for four arbitrarily chosen wavelengths are presented in Fig. 5, where the modulator was biased at -1.0V and the SOA section was biased at 30mA. It should be noted that due to the low output power from the chip, the integrated SOA section was operating within the linear regime, hence it did not influence these measurements. With this in mind, it can be seen that the 3dB bandwidth of the modulator section lies between 5.5 and 6.5GHz depending on the laser tuning settings, which is sufficient for 10Gb/s modulation. However, alongside the use of QWI, we believe that the performance of the modulator section can be significantly improved in future iterations through a reduction in the parasitic capacitance of the RF contact pads through the addition of a low-k dielectric polymer as demonstrated in [16].

C. SOA Section

The integration of an SOA section within the transmitter was originally targeted not only compensate for the intrinsic loss of the modulator but also to provide a gating function necessary for burst-mode operation as demonstrated in [17].

As shown in Figure 2(a), the output facet of the 675μm-long SOA section was angled at 7° with respect to the ridge waveguide to reduce unwanted reflections. However, due to the absence of an anti-reflection (AR) coating, a residual facet reflectivity is responsible for producing FP modes in the amplified spontaneous emission (ASE) spectrum of the SOA section as shown in Fig. 6. In accordance with the model presented in [18], which does not take into account the roughness of the inductively coupled plasma (ICP) etch, this residual facet reflectivity was estimated to be approximately 0.02. It should be noted that we have assumed the same reflectivity for both facets as they were formed during the same etch step and have the same physical properties (i.e. tilt angle, depth). In addition, the ripple observed to encompass the amplitude of the FP modes indicates that the 80μm-long modulator section (separated from the SOA using a shallow 1μm-wide etch) is contained within the ASE resonance cavity, resulting in a total length of 756μm. Nonetheless, as the presence of the FP modes served to degrade the attainable SMSR, it ultimately placed a limit on the achievable output power from this test device. As a result, it is clear that further structural optimization is required for this integrated SOA section in future iterations of this transmitter. For instance, in addition to the use of an AR coating, a modified facet employing tapers or mode expanders may further minimize any undesired optical feedback [19].

For the device-under-test, the SOA bias that provided the optimum trade-off between output power and SMSR was found to be around 30mA. At this bias, the gain available to the lasing wavelengths within the specified tuning range was estimated to be between 10.2dB and 12.7dB using a modified Hakki-Paoli technique proposed in [20] which accounts for the finite resolution bandwidth of the OSA that was set to 0.1nm. Subsequently, by using a Gaussian field approximation and assuming an angular alignment accuracy $\leq 0.15°$ with zero lateral offset, the coupling loss between the chip and the lensed fiber can be as much as 5dB [21]. Taking this value into account and using the estimated gain of the SOA at a test wavelength of 1557.37nm ($\approx$ 11.1dB), which exhibited a

peak fiber-coupled power of -17.5dBm in Fig. 4(c), the power at the output of the modulator can be estimated as -23.6dBm. Additionally, the typical peak power achievable from a discrete 3s-SFP laser is in the range of +5dBm to -5dBm depending on the selected mode, hence by assuming a minimum peak output power of -5dBm, the loss of the modulator section within this test device can be estimated to be 18.6dB. This value suggests that the loss of the modulator section in dB is three or four times the typical value reported for monolithically integrated electro-absorption modulators (EAMs) [2], [22]. Nonetheless, by considering a structural optimization of the modulator section (e.g. through QWI) in order to achieve an insertion loss representative of a typical value (≈ 5dB), the same SOA section should provide a sufficient level amplification at 30mA to achieve a peak output power of roughly +1dBm. However, by accounting for modulation and including a typical fiber coupling loss for packaged devices of 2dB, the achievable output power from the chip would be further reduced by 5dB. Consequently, a larger gain provided by an increased SOA bias could allow higher output powers to be reached such as those required by current PON standards, provided that the residual facet reflectivity is improved with the inclusion of an AR coating. However, as demonstrated in [23], the presence of thermal crosstalk within monolithically integrated devices has the potential to compromise the integrity of the transmission wavelength, hence, it must be investigated.

D. Temperature Dependence and Inter-section Crosstalk

The discrete nature of the lasing modes obtained from the monolithically integrated transmitter demands a novel strategy for local wavelength identification coupled with a technique for fine tuning and stabilization in order to reach and maintain the wavelengths specified by the ITU-T DWDM spectral grid [24]. In particular, as the global temperature plays an important role in defining the resonance conditions of a 3s-SFP laser, the influence of a temperature variation on the set lasing wavelength was studied using two distinct tuning settings for which the peak was monitored as the sub- mount temperature was varied. The corresponding results are shown in Fig. 7. It is important to recognize that depending on the tuning settings, the temperature variation can cause either a linear variation of the wavelength with temperature or a mode-hop. Moreover, if the mode-hop regions are excluded, the temperature dependence of the lasing wavelength can be quantified as approximately 0.17nm/°C. This value is relatively high when compared with the corresponding value obtained for other test devices (~0.11nm/°C), which may be caused by a discrepancy in the material structure. Nevertheless, this dependence can be exploited to complement the tuning achieved by the applied bias currents in order to fine tune and stabilize the wavelength to a desired ITU-T channel through the use of a feedback control loop and an appropriate wavelength referencing strategy. Additionally, in order to examine the impact of inter-section crosstalk, the peak transmission wavelength of an arbitrary tuning setting was monitored using an OSA while the bias supplied to the integrated modulator and SOA sections were varied for a fixed sub-mount temperature of 20°C.

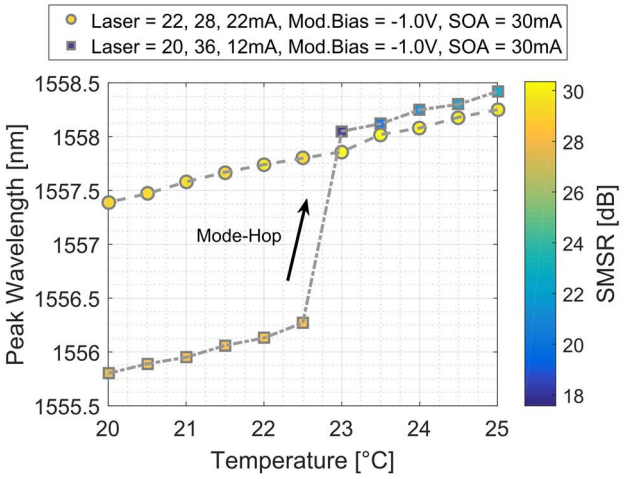

Fig. 7. Temperature dependence of the lasing wavelength.

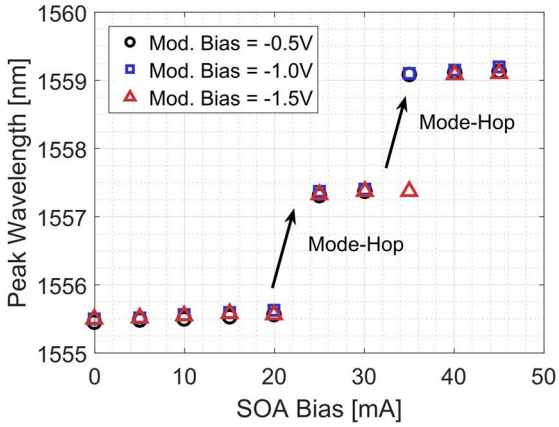

Fig. 8. The impact of crosstalk between the transmitter components captured by varying the applied modulator and SOA bias for a fixed laser tuning bias (22mA, 28mA, 22mA) and sub-mount temperature (20°C)

The results of this analysis are presented in Fig. 8. Notably, the peak wavelength was largely independent of the DC voltage applied to the modulator section; however, increasing the bias current supplied to the SOA section produced an undesirable shift in the peak that occasionally resulted in abrupt mode-hops. As the tuning efficiency observed here is very low, this information suggests that localized heating produced by the SOA section may be shifting the laser cavity closer to the SOA, hence, the resulting cavity misalignment may be the reason for the induced mode hop; however, a residual optical reflection within the cavity may also be a contributing factor. Nonetheless, a thermal interaction between the SOA and laser sections is an undesirable effect that serves to complicate the calibration and tuning of the integrated transmitter in terms of wavelength and output power. However, it is important to recognize that thermal cross-talk is a common feature of all monolithically integrated tunable transmitters [23] and, as outlined previously, bias currents can be found for this test device which provide an optimum trade-off between wavelength tuning SMSR and output power for continuous-mode operation. The effect of thermal cross-talk on the wavelength stability will be further

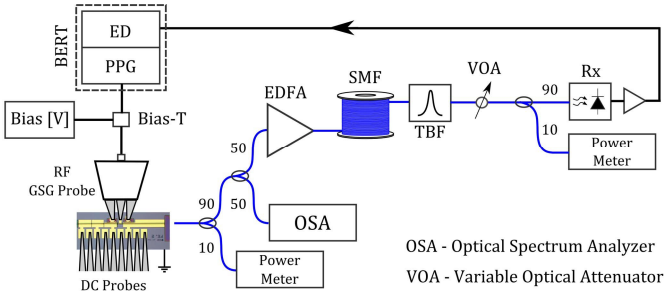

Fig. 9. Experimental setup: 10G continuous-mode transmission tests.

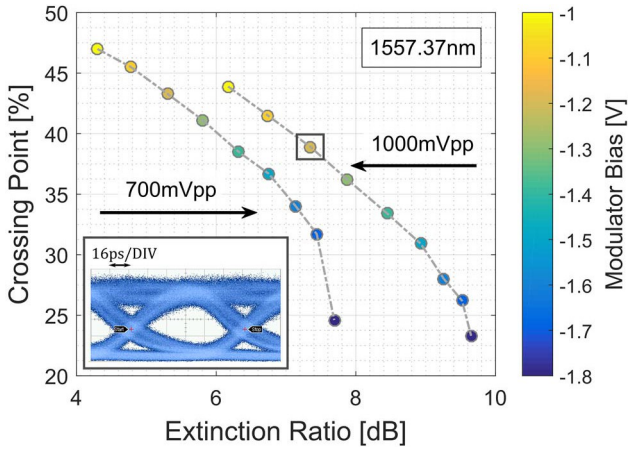

Fig. 10. 10G NRZ-OOK eye crossing point and extinction ratio as a function of the applied modulator bias for a typical lasing mode.

analyzed dynamically in section IV-B which accounts for the pulsed SOA bias current used to emulate burst-mode operation.

E. Continuous-Mode Transmission Performance

To evaluate the transmission capability of the integrated transmitter, the CM performance was investigated for various tuning settings under amplitude modulation at 10Gb/s. The corresponding experimental setup is shown in Fig. 9. At the transmit side, a pulse-pattern generator (PPG) was used to produce a pseudo-random binary sequence (PRBS-7) for NRZ-OOK modulation at 10.3125Gb/s with a peak-to-peak voltage swing of 1V (+500mV). This signal was supplied through a bias-tee to the RF GSG probe connected to the modulator section. The voltage swing supplied by the PPG to the modulator was then optimized in order to achieve the best compromise between the extinction ratio (ER) and eye crossing point; this process is shown in Fig. 10 for a lasing mode located at 1557.37nm. Notably, the observed reduction in the crossing point can be attributed to an appreciable level of non-linear absorption introduced by the modulator section in response to the increased level of reverse bias. Moreover, as the insertion loss of the trial modulator structure resulted in an appreciably low fiber-coupled output power from the unpackaged chip, a gain-stabilized erbium-doped fiber amplifier (EDFA) was used to boost the power of the signal launched into the transmission fiber for all the test wavelengths to a value close to +5dBm which is comparable

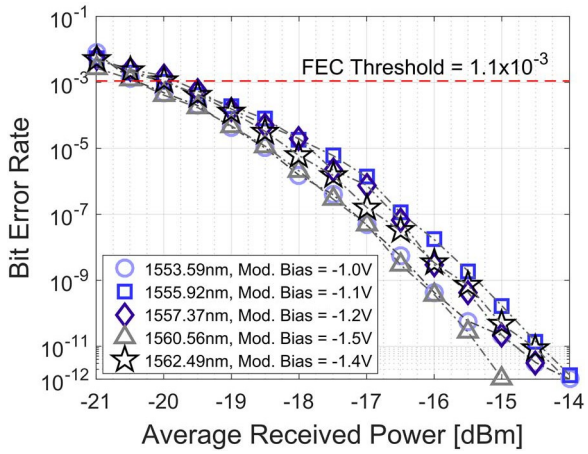

Fig. 11. Back-to-back transmission performance of 5 lasing modes using an optimized modulator bias.

with devices specified for current PON standards [11]. At the receiver (Rx) side, a tunable bandpass filter (TBF) with a 3dB passband of 0.5nm was used to remove the excess out-of-band amplified spontaneous emission (ASE) while a variable optical attenuator (VOA) was used to control the average power of the signal entering the commercial 12.5GHz PIN-based photo-receiver (Rx). An electrical amplifier with an effective gain of 14dB was then used to optimize the electrical signal from the Rx for use with the error detector (ED) which has a minimum sensitivity of 50mV peak-to-peak.

Multiple lasing modes with an SMSR ≥ 30dB were tested in back-to-back at 10Gb/s, five of which are presented in Fig. 11. These measurements demonstrate error-free transmission (BER ≤ 1E-12) with a residual sensitivity variation of 0.5dB around the forward error correction (FEC) threshold of 1.1E-3 [25] which can be attributed to a slight difference in the ER achieved for each mode. In addition, the performance of the transmitter was also examined using 20km and 50km of standard SMF; the results of this analysis are presented in Fig. 12 using a test wavelength at 1557.37nm (SMSR ≈ 34dB). It should be noted that as the bias applied to the integrated modulator section has been adjusted to optimize the signal quality for each transmission length, the penalty observed in Fig. 12 may appear exaggerated. For instance, the performance quoted for commercial devices typically involves optimizing the applied bias for a certain transmission distance and comparing the resulting BER performance with the back-to-back measurement taken at the same bias. In this case, the penalty would appear smaller, but only because the back-to-back performance is not optimized. In addition, adjusting the modulator bias for the exact distance in a real deployment scenario may not be feasible in large volume, low-cost transmitters, hence it is important to note that the results presented here simply serve to indicate the entire transmission performance capabilities of the transmitter. Nonetheless, based on these initial results, it is expected that future iterations of the integrated transmitter which incorporate an optimized modulator design to enable an improved output power will be capable of achieving error-free transmission in

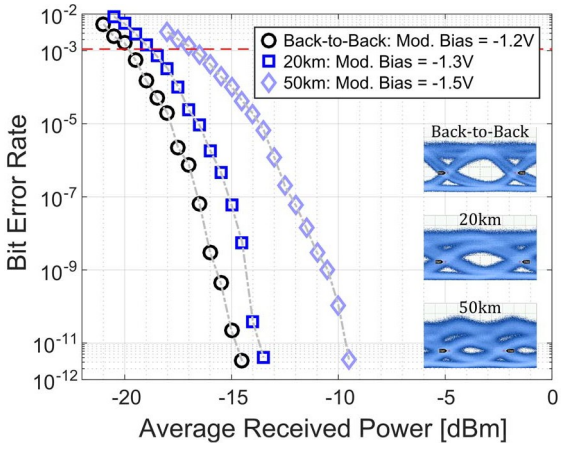

Fig. 12. Transmission performance comparison at 1557.37nm using an optimized modulator bias [Back-to-back, 20km and 50km]

the absence of dispersion compensation for fiber lengths which encompass the typical physical reach targeted by current PON standards [11].

IV. Wavelength Stability: Signal Modulation and Optical Burst Generation

In order to investigate the wavelength stability of the integrated transmitter during data transmission, a time-resolved chirp measurement technique was employed using a programmable optical bandpass filter as a frequency discriminator. The basic theoretical background for the measurement process is presented here; however, for a more detailed description the reader is referred to [26]. The corresponding experimental setup is shown in Fig. 13.

In this experiment, a programmable optical filter based on high-resolution liquid-crystal-on-silicon (LCoS) technology was employed as a frequency discriminator with a transfer function, $H(\omega)$,designed to be linear in magnitude around the carrier frequency, ω_c, with a transmission amplitude, T_0, and differential coefficient, c_1:

$$H(\omega) = T_0[1 \pm 2\pi c_1(\omega - \omega_c)] \quad (1)$$

As outlined in [26], c_1 is typically complex and dependent on frequency where the imaginary part gives the chromatic dispersion of the filter. However, in this work, the use of a programmable filter enables c_1 to be set as a real value that is defined by the frequency discriminator bandwidth ($f_{BW} = \omega_{BW}/2\pi$) which specifies the frequency range bounded by transmission values of 0.1 and 0.9 where the center carrier frequency has a transmission of 0.5.

$$c_1 = \frac{(0.9 - 0.1)}{(0.5).2\pi . f_{BW}} \quad (2)$$

This approach enables the sensitivity of the measurement to be adjusted in order to capture chirp traces with amplitudes ranging from a few GHz to approximately 100GHz. Consequently, by adjusting the filter profile, as shown in Fig. 14, two optical power waveforms P_+ and P_- can be obtained when

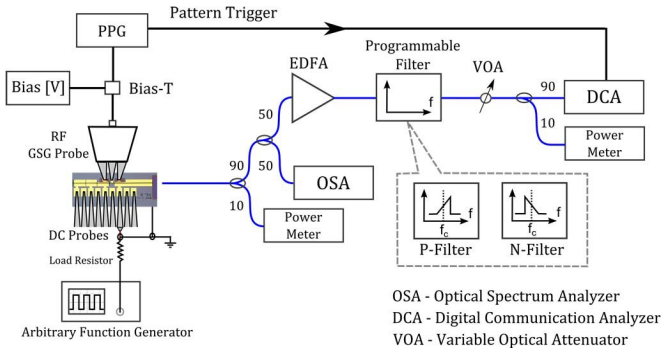

Fig. 13. Experimental setup: Time-resolved chirp measurement using a programmable optical filter.

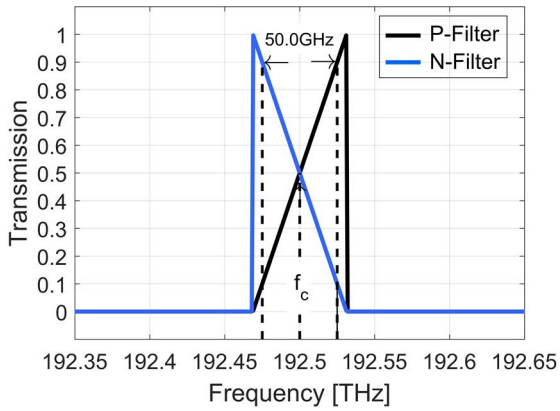

Fig. 14. Optical filter profiles used for frequency discrimination. (P-Filter: Filter with positive slope, N-Filter with negative slope).

the filter slope is positive and negative respectively. From this data two additional values can be derived as

$$P_{AM} = \frac{P_+ + P_-}{2} = T_0{}^2 P_{in} \quad (3)$$

$$P_{FM} = \frac{P_+ - P_-}{2} = 2T_0{}^2 P_{in} c_1 \frac{d\varphi}{dt} \quad (4)$$

where, P_{AM} is the amplitude modulation, P_{FM} gives the power profile produced by carrier-induced frequency variations and P_{in} represents the optical power incident on the filter.

The frequency chirp, $\Delta\nu$, can then be derived as

$$\Delta\nu = \frac{1}{2\pi}\frac{d\varphi}{dt} = \frac{1}{4\pi c_1}\frac{P_{FM}}{P_{AM}} \quad (3)$$

where, φ is the slowly time-varying phase of the optical signal's electric-field.

A. Chirp Contribution from the Modulator Section

The chirp contribution from the modulator section was examined at 10Gb/s with NRZ-OOK modulation using two distinct data patterns. The first consisted of alternating 1's and 0's in order to examine the impact of high frequency data transitions on the carrier frequency while the second pattern contained a lower frequency content consisting of an alternating sequence of 64 1's followed by 64 0's. For example,

TABLE I

CHIRP CONTRIBUTION FROM THE MODULATOR SECTION USING THE HIGH FREQUENCY NRZ-OOK TEST PATTERN

Peak Lasing Wavelength [nm]	Modulator Bias [V]	Peak-to-Peak Chirp [GHz]
1553.59	-1.0	3.45
1555.92	-1.1	2.99
1557.37	**-1.2**	**1.96**
1562.49	-1.4	3.69

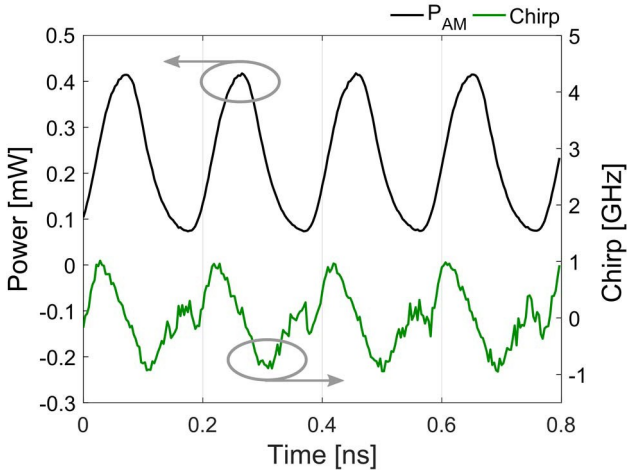

Fig. 15. P_{AM} and chirp traces for 10G NRZ-OOK modulation using the high frequency '101010' test pattern for an applied modulator bias of −1.2V [Center wavelength ≈ 1557.37nm, SOA bias = 30mA].

the peak-to-peak chirp ($\Delta\nu_{pp}$) obtained from four different laser tuning settings using the high frequency test pattern are presented in Table I. In each case, the reverse bias applied to the modulator has been set with the optimum value for back-to-back CM transmission while the voltage swing was set at 500mV as this was found to provide the optimum ER as demonstrated in Fig. 10. The corresponding P_{AM} and chirp traces at a set center frequency of 192.5THz (1557.36nm) are presented in Fig. 15 for an applied modulator bias of 1.2V. Notably, the chirp dynamics demonstrate a positive frequency deviation at the leading edge of the pulse followed by a negative deviation on the trailing edge indicating that the chirp is positive for this value of reverse bias.

The subsequent results obtained using the low frequency test pattern are presented in Fig. 16. Here, $\Delta\nu_{pp}$ is presented as a function of the applied modulator bias where the laser and SOA sections have been maintained at fixed values. In particular, there is an appreciable increase in $\Delta\nu_{pp}$ as the value of reverse bias applied to the modulator section is increased beyond -1.3V. For comparison with the results presented in Fig. 15, the chirp trace obtained using the low frequency pattern for an applied modulator bias of -1.2V is presented in Fig. 17. From these results, it is evident that

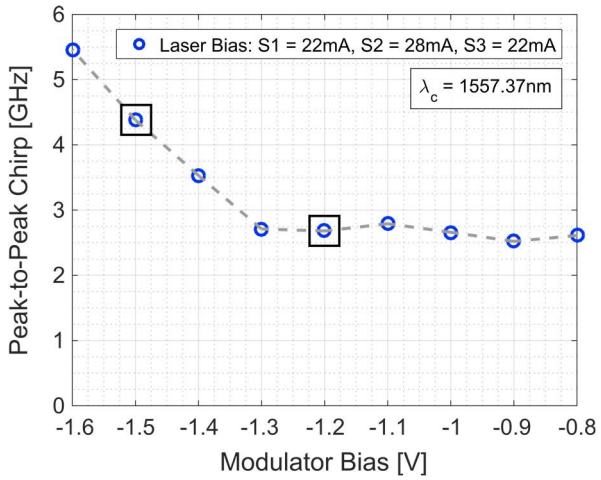

Fig. 16. Peak-to-peak chirp contribution from the modulator section using the low frequency test pattern [64 × '1' + 64 × '0'] for a fixed laser and SOA bias [Center wavelength ≈ 1557.37nm, SOA bias = 30mA]

the chirp dynamics are more complex for the low frequency test pattern due to the presence of an adiabatic contribution which may be the result of optical feedback as discussed in Section III-C. Nonetheless, the chirp dynamics clearly exhibit a negative frequency excursion at the trailing edge of each pulse which suggests a positive chirp as observed for the high frequency pattern at the same modulator bias. Alternately, for a larger modulator bias of -1.5V, as shown in Fig. 18, the chirp demonstrates a substantial negative frequency excursion at the leading edge of the pulse alongside a subtle positive deviation the trailing edge. Notably, this feature increases as the reverse bias is increased further, resulting in the trend observed in Fig. 16. This response also suggests that the sign of the chirp has flipped from positive to negative; however, as a detailed analysis of the chirp dynamics falls beyond the scope of this work, this investigation is left for further study. Nonetheless, this behavior can be an advantageous as negatively chirped pulses undergo compression due to chromatic dispersion within standard SMF [27], [28]. In other words, pulses exhibiting the type of chirp demonstrated in Fig. 18 are desirable for networks requiring transmission over a longer physical reach. It is also important to note that this value of bias (-1.5V) corresponds to the setting required to optimize the signal performance for transmission over 50km of fiber in Fig. 12. Moreover, the observed peak-to-peak frequency deviation (≤ 6GHz) is well within the maximum spectral excursion of ±12.5GHz targeted by current PON standards for systems employing a 50GHz channel spacing [11].

B. *Carrier Frequency Deviation Induced By Dynamic Operation of the Integrated SOA*

For upstream transmission within a dynamic TDM-DWDM PON, each ONU is required to transmit data within an allocated timeslot in order to avoid data collisions over the shared network infrastructure. These packets of data can be successfully generated using an SOA to carve the required optical envelopes [29]. Compared to other methods to generate

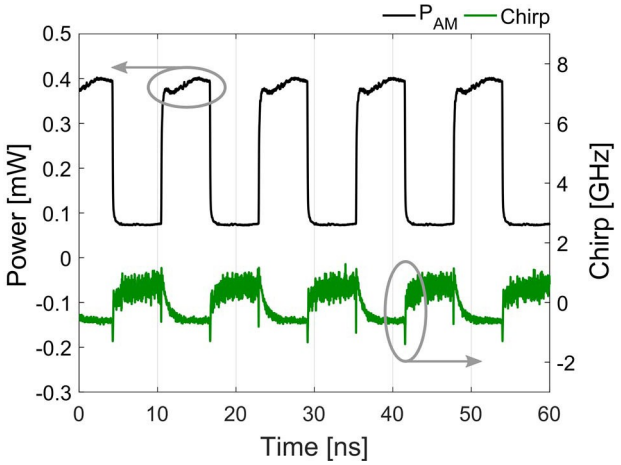

Fig. 17. P_{AM} and chirp traces for 10G NRZ-OOK modulation using the low frequency test pattern for an applied modulator bias of -1.2V. [Center wavelength $\approx$ 1557.37nm, SOA bias = 30mA]

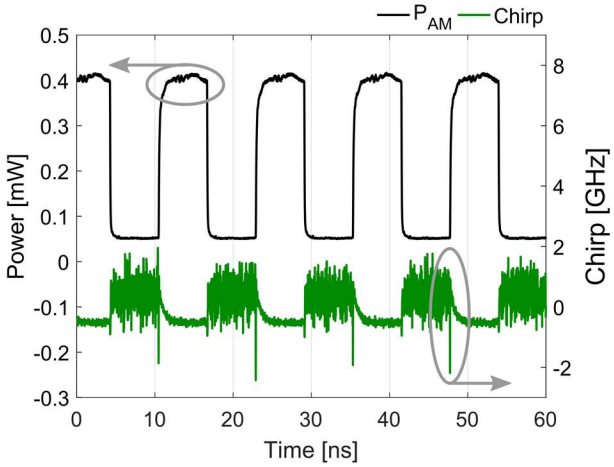

Fig. 18. P_{AM} and chirp traces for 10G NRZ-OOK modulation using the low frequency test pattern for an applied modulator bias of -1.5V [Center wavelength $\approx$ 1557.37nm, SOA bias = 30mA].

the optical bursts, the use of gating SOAs has the advantage that laser can be left in the on-state, which simplifies the problem of maintaining the wavelength stability. For instance, the main approach used to generate optical bursts within single-channel PONs involves gating the bias of directly modulated lasers (DMLs), however, this process introduces an appreciable frequency drift that is currently a significant performance limiting issue for the current multi-channel PON standards [11], [30].

The wavelength stability of the integrated transmitter for burst-mode operation was investigated using the time-resolved chirp measurement technique also used to examine variations in the unmodulated carrier frequency induced by the dynamic performance of the integrated SOA. As shown in Fig. 13, a programmable function generator (FG) was connected to the SOA section of the transmitter to facilitate the generation of the burst envelopes. In addition, a load resistance was connected in series with the SOA section in order to match the output impedance (50Ω) of the FG and maximize the power transfer to the device. The voltage-current (V-I) profile obtained from the SOA section under different operating conditions is presented in Fig. 19. These results show that with injected light, the threshold voltage of the SOA section is increased from roughly 650mV to approximately 800mV due to depletion of the excited carrier density by stimulated emission and an appreciable thermal influence that can be attributed to the laser section. It is also important to note that the reverse bias applied to the modulator section did not have an observable impact on the V-I profile of the neighboring SOA section and hence we can assume that there is negligible electrical crosstalk between these components.

The voltages applied to the SOA in order to generate the burst envelopes were 1.33V (V_{High}) and 0.9V (V_{Low}). The value of V_{High} was chosen as it corresponds to a bias current of 30mA which provided the best trade-off between SMSR and output power during the DC characterization while the value of V_{Low} was chosen in an attempt to maximize the on/off power ratio of the SOA section through the application of a

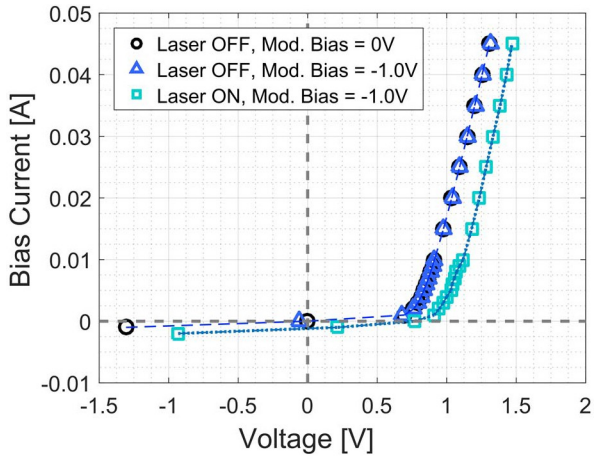

Fig. 19. V-I profile of the SOA section demonstrating a threshold shift with injected light at 1556.51nm [Laser bias = 25mA, 30mA and 40mA]

reverse bias. For DC operation, the extinction provided by the SOA section under these bias conditions was measured to be approximately 27dB.

For the purpose of this analysis, a square wave signal with a rise/fall time of 5ns and a duty cycle of 50% was applied to the SOA section and its frequency was varied coarsely from 100Hz to 100kHz. While it should be recognized that these gating conditions are unlikely to occur in a real deployment scenario, they represent extreme cases that can help in analyzing the internal behavior of the transmitter. The corresponding deviation of the carrier frequency was measured using optical filters similar to that presented in Fig. 14. However, for these measurements the passband (f_{BW}) was increased to 100GHz.

The measured peak-to-peak frequency deviation is presented in Fig. 20 as a function of the applied SOA gating period. This data indicates that the deviation is fairly constant (< 8GHz) for gating frequencies above 10kHz which is comparable with typical burst durations of 125μs as required by current PON standards [31]. However, as the gating frequency is decreased the carrier frequency deviation begins to increase

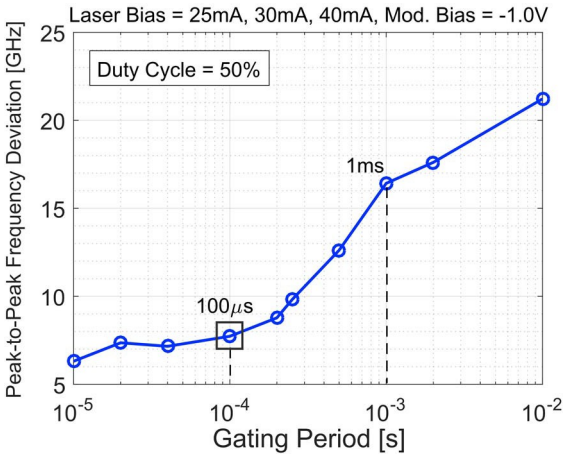

Fig. 20. Peak-to-peak carrier frequency deviation induced by a square-wave gating signal with a 50% duty cycle applied to the SOA Section. ($\lambda_c \approx$ 1556.51nm).

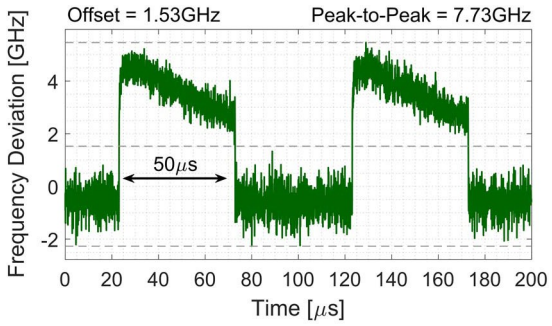

Fig. 21. Frequency deviation induced by a 10kHz square-wave signal with a 50% duty cycle applied to the SOA section. [Center filter frequency = 192.605THz (1556.51nm), f_{BW} = 100GHz]

rapidly reaching a value of approximately 22GHz for a gating frequency of 100Hz. This trend is in line with the assumption that thermal crosstalk associated with the bias applied to the SOA section can be significant enough to perturb the set carrier frequency as initially presented in Fig. 8, which examined the wave length stability of the transmitter for a constant SOA bias. However, the timescales of the heat transfer between the SOA and the laser sections are extremely important in order to understand the dynamic operation of this monolithically integrated transmitter. For instance, as shown in Fig. 21, the frequency deviation presents fast transients at the leading and trailing edges of the gating signal with timescales below 1μs for burst durations up to around 50μs. We believe that this fast wavelength deviation might not be related to heat transfer, which is usually a slower effect, and might be due to the residual cavity interaction between the SOA and the laser. For bursts durations above 100μs the heat transfer becomes the dominant factor causing the large wavelength deviations measured dynamically in Fig. 20 and statically in Fig. 8.

These results suggest that for typical PON burst durations of up to 125μs, the heat generated by the SOA section in the ON state does not have the time to transfer substantially into the laser section, maintaining a relatively small wavelength drift of around 8GHz. This is an interesting result as it represents a highly desirable feature for low-cost tunable transmitters for use in wavelength agile PONs and shows the advantages of an integrated transmitter employing a separate SOA section to perform the burst gating function. As mentioned earlier, directly modulated lasers (DMLs) which are presently of high interest for deployment in ONU transmitters [32], present an appreciable burst-mode induced frequency drift that is currently a significant performance limiting issue as the applied gating function can severely impact the carrier-induced refractive index. Nonetheless further investigations are essential in order to optimize the integration of better understand the heat transfer in the proposed integrated structure in order to improve the overall performance of this device in future iterations.

V. Conclusions

This work outlines the initial progress towards developing a potentially low-cost monolithically integrated tunable 10G transmitter consisting of a slotted Fabry-Pérot laser, and absorptive modulator and an SOA targeted for deployment within the ONUs of wavelength agile PONs. The transmitter structure is primarily driven by the substantial cost savings that can be achieved through the use of efficient re-growth free fabrication techniques that facilitate monolithic integration, by defining lithographically the various components.

The first iteration of this tunable transmitter was produced using an 'off-the-shelf' AlInGaAs/InP MQW structure on an n-doped substrate and following a coarse calibration it demonstrated a discrete single-mode tuning range of approximately 12nm between 1551 and 1563nm with an SMSR $\geq$ 30dB. Using an external amplifier to counteract the excess insertion loss introduced by the trial modulator structure and the fiber coupling loss attributed to the experimental setup, error-free (BER $\leq$ 1E-12) transmission was achieved using NRZ-OOK modulation at 10Gb/s with a PRBS-7 pattern for fiber lengths up to 50km which encompasses the physical reach targeted by the latest PON standards. Furthermore, in order to determine the inherent wavelength stability of the transmitter, a time-resolved chirp measurement technique was used to examine deviations in the set carrier frequency induced by modulation and the dynamic operation of the integrated SOA section. Notably, the modulator section demonstrated a chirp contribution of < 6GHz for NRZ-OOK modulation at 10Gb/s using test patterns with high and low frequency content. Furthermore, the application of a gating function to the SOA section to emulate the generation of optical bursts was found to shift the unmodulated carrier frequency of a typical lasing mode by $\leq$ 8GHz when the gating period was comparable with typical PON bursts durations of 125μs which is faster than the thermal response time of the transmitter material. These recorded values are significantly better than those currently achievable from ONU transmitters utilizing directly modulated lasers (DMLs) in the absence of active chirp compensation [32]; however, despite the challenges facing future iterations of this device, the experimental results presented in this work ultimately serve to highlight the advantages offered

by monolithic integration coupled with low-cost, re-growth-free fabrication processes.

ACKNOWLEDGMENTS

The authors would like to gratefully acknowledge the financial support provided by Science Foundation Ireland (SFI) (grants 12/IA/1270 and 12/RC/2276), and by the EU FP7 project DISCUS (grant CNECT-ICT-318137).

REFERENCES

[1] M. Ruffini *et al.*, "DISCUS: An end-to-end solution for ubiquitous broadband optical access," IEEE *Commun. Mag.*, vol. 52, no. 2, pp. S24–S32, Feb. 2014.

[2] B. Mason, G. A. Fish, S. P. DenBaars, and L. A. Coldren, "Widely tunable sampled grating DBR laser with integrated electroabsorption modulator," *IEEE Photon. Technol. Lett.*, vol. 11, no. 6, pp. 638–640, Jun. 1999.

[3] H. Ishii, H. Tanobe, F. Kano, Y. Tohmori, Y. Kondo, and Y. Yoshikuni, "Quasicontinuous wavelength tuning in super-structure-grating (SSG) DBR lasers," *IEEE J. Quantum Electron.*, vol. 32, no. 3, pp. 433–441, Mar. 1996.

[4] A. J. Ward *et al.*, "Widely tunable DS-DBR laser with monolithically integrated SOA: Design and performance," *IEEE J. Sel. Topics Quantum Electron.*, vol. 11, no. 1, pp. 149–156, Jan. 2005.

[5] R. Laroy, G. Morthier, T. Mullane, M. Todd, and R. Baets, "Stabilisation and control of widely tunable MG-Y lasers with integrated photodetectors," *IET Optoelectron.*, vol. 1, no. 1, pp. 35–38, Feb. 2007.

[6] B. Mroziewicz, "External cavity wavelength tunable semiconductor lasers—A review," *Opto-Electron. Rev.*, vol. 16, no. 4, pp. 347–366, 2008.

[7] C. Gierl *et al.*, "Surface micromachined tunable 1.55 μm-VCSEL with 102 nm continuous single-mode tuning," *Opt. Express*, vol. 19, no. 18, pp. 17336–17343, 2011.

[8] W. T. Tsang, N. A. Olsson, R. A. Linke, and R. A. Logan, "1.5 μm wavelength GaInAsP C3 lasers: Single-frequency operation and wideband frequency tuning," Electron. *Lett.*, vol. 19, no. 11, pp. 415–417, May 1983.

[9] O. Hildebrand, W. Idler, K. Dutting, G. Laube, and K. Wunstel, "The Y-laser: A multifunctional device for optical communication systems and switching networks," *J. Lightw. Technol.*, vol. 11, no. 12, pp. 2066–2075, Dec. 1993.

[10] K. Shi *et al.*, "Characterization of a novel three-section tunable slotted Fabry–Perot laser," in *Proc. Conf. Opt. Fiber Commun., Nat. Fiber Opt. Eng. Conf. (OFC/NFOEC)*, San Diego, CA, USA, Mar. 2010, pp. 1–3.

[11] International Telecommunications Union—Radiocommunication (ITU-R), Recommendation G.989.2, "40-Gigabit-Capable Passive Optical Networks 2 (NG-PON2): Physical Media Dependent (PMD) Layer Specification." [Online]. Available: https://www.itu.int/rec/T-REC-G.989.2-201412-I/en

[12] K. Shi *et al.*, "Characterization of a tunable three-section slotted Fabry–Perot laser for advanced modulation format optical transmission," *Opt. Commun.*, vol. 284, no. 6, pp. 1616–1621, Mar. 2011.

[13] J. Zhao, K. Shi, Y. Yu, and L. P. Barry, "Theoretical analysis of tunable three-section slotted Fabry–Perot lasers based on time-domain traveling-wave model," *IEEE J. Sel. Topics Quantum Electron.*, vol. 19, no. 5, Sep./Oct. 2013, Art. no. 1503108.

[14] P. Ramaswamy, B. Roycroft, J. O'Callaghan, C. L. Janer, F. H. Peters, and B. Corbett, "Wavelength agile slotted Fabry–Pérot lasers," in *Proc. Int. Semiconductor Laser Conf.*, Palma de Mallorca, Spain, Sep. 2014, pp. 102–103.

[15] S.-W. Shen, G.-Y. Li, Z.-Y. Lin, C.-K. Lee, and Y.-J. Chiu, "Power-enhancement broadband cascaded integration of electroabsorption modulator and semiconductor optical amplifier by local quantum well intermixing," in *Proc. IEEE Photon. Conf.*, San Diego, CA, USA, Oct. 2014, pp. 278–279.

[16] Y. Cheng *et al.*, "40-Gb/s low chirp electroabsorption modulator integrated with DFB laser," *IEEE Photon. Technol. Lett.*, vol. 21, no. 6, pp. 356–358, Mar. 15, 2009.

[17] K. Taguchi, K. Asaka, S. Kimura, K.-I. Suzuki, and A. Otaka, "Reverse bias voltage controlled burst-mode booster SOA in λ-tunable ONU transmitter for high-split-number TWDM-PON," *J. Opt. Commun. Netw.*, vol. 10, no. 4, pp. 431–439, Apr. 2018.

[18] D. Marcuse, "Reflection loss of laser mode from tilted end mirror," *J. Lightw. Technol.*, vol. 7, no. 2, pp. 336–339, Feb. 1989.

[19] I. F. Lealman, L. J. Rivers, and S. D. Perrin, "InGaAsP/InP tapered active layer multiquantum well laser with 1.8 dB coupling loss to cleaved singlemode fibre," *Electron. Lett.*, vol. 30, no. 20, pp. 1685–1687, Sep. 1994.

[20] L. D. Westbrook, "Measurements of dg/dN and dn/dN and their dependence on photon energy in λ = 1.5 μm InGaAsP laser diodes," *IEE Proc. J-Optoelectron.*, vol. 133, no. 2, pp. 135–142, Apr. 1986.

[21] S. Yuan and A. N. Riza, "General formula for coupling-loss characterization of single-mode fiber collimators by use of gradient-index rod lenses," *Appl. Opt.*, vol. 38, no. 15, pp. 3214–3222, 1999.

[22] G. Talli, A. Naughton, S. Porto, C. Antony, P. Ossieur, and P. D. Townsend, "Advantageous effects of gain saturation in semiconductor optical amplifier-based integrated reflective modulators," *J. Lightw. Technol.*, vol. 32, no. 3, pp. 392–401, Feb. 1, 2014.

[23] P. Kozodoy *et al.*, "Thermal effects in monolithically integrated tunable laser transmitters," *IEEE Trans. Compon. Packag. Technol.*, vol. 28, no. 4, pp. 651–657, Dec. 2005.

[24] International Telecommunications Union—Radiocommunication (ITU-R), Recommendation G.694.1, "Spectral Grids for WDM Applications: DWDM Frequency Grid." [Online]. Available: https://www.itu.int/rec/T-REC-G.694.1-201202-I/en

[25] International Telecommunications Union—Radiocommunication (ITU-R), Recommendation G.975, "Forward error correction for submarine systems." [Online]. Available: https://www.itu.int/rec/T-REC-G.975-200010-I/en

[26] K. Sato, S. Kuwahara, and Y. Miyamoto, "Chirp characteristics of 40-Gb/s directly modulated distributed-feedback laser diodes," *J. Lightw. Technol.*, vol. 23, no. 11, pp. 3790–3797, Nov. 2005.

[27] F. Dorgeuille and F. Devaux, "On the transmission performances and the chirp parameter of a multiple-quantum-well electroabsorption modulator," *IEEE J. Quantum Electron.*, vol. 30, no. 11, pp. 2565–2572, Nov. 1994.

[28] M. Y. Jamro and J. M. Senior, "Optimising negative chirp of an electroabsorption modulator for use in high-speed optical networks," *Eur. Trans. Telecommun.*, vol. 18, no. 4, pp. 369–380, 2007.

[29] G. Talli *et al.*, "SDN enabled dynamically reconfigurable high capacity optical access architecture for converged services," *J. Lightw. Technol.*, vol. 35, no. 3, pp. 550–560, Feb. 1, 2017.

[30] G. Simon *et al.*, "Focus on time-dependent wavelength drift of DMLs under burst-mode operation for NG-PON2," *J. Lightw. Technol.*, vol. 34, no. 13, pp. 3148–3154, Jul. 1, 2016.

[31] International Telecommunications Union—Radiocommunication (ITU-R), Recommendation G.989.3.1, "40-Gigabit-capable passive optical networks (NG-PON2): Transmission convergence layer specification." [Online]. Available: https://www.itu.int/rec/T-REC-G.989.3/e

[32] Y. Matsui *et al.*, "Transceiver for NG-PON2: Wavelength tunablity for burst mode TWDM and point-to-point WDM," in *Proc. Opt. Fiber Commun. Conf. Exhibit. (OFC)*, Anaheim, CA, USA, Mar. 2016, pp. 1–3.

Daniel Carey received the B.Sc. degree in physics from University College Cork, Ireland, in 2011, where he is currently pursuing the Ph.D. degree in physics with the Photonic Systems Group, Tyndall National Institute, under the supervision of Prof. P. Townsend. He is a member of the Photonic Systems Group, Tyndall National Institute, University College Cork. His research is focussed on the realization of dynamically reconfigurable long-reach passive optical networks through physical layer design and subsystems analysis.

Prasanna Ramaswamy received the bachelor's degree in engineering physics from IIT Madras, Chennai, India, in 2010. In 2010, he went on to do the Erasmus Mundus Master of Science in photonics from Ghent University and Vrije Universiteit Brussel, Belgium, and the KTH Royal Institute of Technology, Stockholm, Sweden. He is currently pursuing the Ph.D. degree with the Tyndall National Institute, Cork, Ireland, with a focus on monolithic integration of tunable lasers and other optical components for telecommunication applications.

Giuseppe Talli received the Laurea degree in electronic engineering from the University of Padova, Italy, in 2000, and the Ph.D. degree in electronic engineering from the University of Essex, U.K., in 2003. From 2004 to 2008, he has been with the Photonic Systems Group, Tyndall National Institute, University College Cork, Ireland, as a Post-Doctoral Scientist. From 2008 to 2012, he has been with Intune Networks Dublin, where he was involved in design and implementation of photonic subsystems for optical burst switching in metro networks. Since 2012, he has re-joined the Tyndall National Institute as a Staff Research Scientist, where he is currently involving in the area of next generation optical access networks, including metro-scale passive optical network architectures and burst-mode subsystems.

Cleitus Antony (M'09) received the B.E. degree in electrical engineering and the M.Sc. degree in physics from the Birla Institute of Technology and Science, Pilani, India, in 2001, and the Ph.D. degree in physics from the Photonics Systems Group, Tyndall National Institute and the Department of Physics, University College Cork, Cork, Ireland, in 2011. During his Ph.D. degree, he was engaged in developing novel burst-mode transmission techniques at data rates of 10 Gb/s in long-reach passive optical networks. From 2001 to 2006, he was with Opnext Japan, Inc., Yokohama, Japan, where he was involved in the design and development of fiber-optic transceivers conforming to the 100-Gbit Ethernet standard. He is currently a Senior Post-Doctoral Researcher with the Photonics Systems Group, Tyndall National Institute, where his research activities include next-generation optical access networks and fiber-optic distributed sensors. He holds five patents in the field of optical telecommunications and has authored more than 40 peer-reviewed publications.

Brendan Roycroft has been with the Tyndall National Institute, Ireland, since 2001. His research interests include designing and testing photonic integrated circuits involving novel telecoms lasers, silicon photonic waveguides and photodetectors, and green and red resonant cavity LEDs, and red and near infra-red VCSELs. Current projects also include developing optical coherence tomography combining several imaging modalities for endoscopes in medical applications, and high precision optical metrology for manufacturing.

Brian Corbett received the B.A. Mod. degree in experimental physics and mathematics and the M.Sc. degree in theoretical physics from the Trinity College, Dublin, Ireland. Since 1991, he has been at the Tyndall National Institute, University College Cork, Cork, Ireland, where he is currently researching the physics and technology of III–V-based light-emitting semiconductors. His research interests include design, fabrication, integration, and characterization of photonic devices with a special emphasis on the use of structuring technologies to add additional function to the device and in using transfer printing to perform the integration. The devices are based on InP, GaAs, GaN, Si, and Ge materials.

Paul D. Townsend received the Ph.D. degree in physics from the University of Cambridge in 1986. He subsequently held a joint position as a Post-Doctoral Fellow at Bellcore, USA, and St. John's College, Cambridge, before joining BT Laboratories, U.K., as a Senior Research Scientist in 1990. In 2000, he joined the Corning Research Centre, U.K., as a Research Associate, with responsibility for access network research and in 2003 moved to the Tyndall National Institute to help create a new photonic systems research activity in Ireland. He is currently the Head of the Photonics Centre and the Photonic Systems Group, Tyndall National Institute, the Director of the Irish Photonic Integration Centre, and a Research Professor with the Department of Physics, University College Cork. The Tyndall Photonics Centre comprises nine internationally recognised research teams (around 140 staff and Ph.D. students in total) carrying out research and development and commercialisation activities spanning the areas of semiconductor materials and devices, photonic integration and packaging, through to advanced photonic systems for telecommunications and healthcare applications. He has authored or co-authored more than 190 journal and conference papers, of which 35 invited, and has 16 patent applications granted or pending. He is a fellow of the Institute of Physics and an Honorary Professor at Herriot-Watt University, Edinburgh.